Petroleum Science 22 (2025) 413–429

Contents lists available at ScienceDirect

Petroleum Science

journal homepage: www.keaipublishing.com/en/journals/petroleum-science

Original Paper

A novel self-rotating down-the-hole hammer with impact and rotary functions for directional drilling: Design, modeling, and experiments

Jin-E Cao, Hong-Yu Cao, Hong-Yun Zhang, Jin-He Bai, Pin-Lu Cao *

College of Construction Engineering, Jilin University, No.938 Ximinzhu Str., Changchun, 130061, Jilin, China

ARTICLE INFO

Article history:
Received 29 April 2024
Received in revised form
11 December 2024
Accepted 11 December 2024
Available online 14 December 2024

Edited by Jia-Jia Fei

Keywords:
Self-rotating pneumatic hammer
Directional drilling
Fluent CFD simulation
Experimental verification

ABSTRACT

Pneumatic down-the-hole hammer, serving as rock-breaking tool, possesses appeal for directional drilling due to its high rate of penetration. However, corresponding experimental studies on existing hammers for directional drilling have rarely been reported, and a model for evaluating their output performance is absent. This study proposes a novel structure of self-rotating pneumatic hammer (NSH) with a built-in rotational mechanism, which converts partial impact energy of the piston to rotate the drill bit and, consequently, enables dual functions of impact and rotate drill bit. The energy is converted via a screw key-groove mechanism, and the wedge-shaped teeth mechanism ensures that the drill bit rotates clockwise during the piston moves downward. The computational fluid dynamics method is applied to simulate the dynamic response of airflow and piston during the operation of Φ127NSH. Meanwhile, a test bench is established to record data concerning chamber pressure and piston displacement, as well as recording its operational status and rock fragmentation during drilling into granite. The results showed that the maximum error between simulated and experimental data is 8.2%. The Φ127NSH successfully achieves dual impact and rotary drilling functions, and granite smoothly feeds and forms a continuous shear rock zone. In addition, the effects of torque load, engagement distance in rotation sleeves, and well deviation angle towards the performance of NSH were studied in detail. The designed Φ127NSH operates at an impact velocity of 3.98 m/s, impact frequency of 12.55 Hz, and rotational speed of 29.51 r/min under a mass-flow rate of 0.18 kg/s, torque load of 400 N·m, engagement distance of 40 mm, and well deviation angle of 0°. The torque load adversely affects the NSH output performance. Increasing the engagement distance improves impact performance while reducing rotational performance. The performance variation of the NSH is minimal when drilling directional wells with varying deviation angles.

© 2024 The Authors. Publishing services by Elsevier B.V. on behalf of KeAi Communications Co. Ltd. This is an open access article under the CC BY-NC-ND license (http://creativecommons.org/licenses/by-nc-nd/4.0/).

1. Introduction

Directional drilling, a technique employed to drill along a predesigned trajectory, is extensively utilized in oil and gas exploration (Inglis, 2013; Li et al., 2020). Its application is expanding gradually to drill into deeper formations that are harder and more complex, driven by the ever-increasing energy demands (Ma et al., 2016; Xi et al., 2022). However, positive displacement motor (PDM), commonly used as down-hole motor for directional drilling, relies on weight-on-bit (WOB) and torque to break up the formations, and experiences a rapid decrease in rate of penetration (ROP) as formation strength increases (Bui et al., 1997). The primary goal of drilling is to drill rapidly to the target (Barbosa et al., 2019). Therefore, it is particularly urgent to develop a high-ROP down-hole motor for directional wells.

Pneumatic down-the-hole (DTH) hammer drilling, on the one hand, relies on the hammer to deliver impact energy into the formation to break it up (Kondratenko et al., 2016; Chervov, 2020). This is achieved by utilizing the high-pressure gas output from the air compressor to drive the reciprocating movement of the piston inside the hammer, seen in Fig. 1. The strength of most rocks, especially brittle ones, diminishes under such impact energy, and, consequently, significantly increasing the ROP compared to conventional methods reliant on weight-on-bit to break rock (Li et al., 2021a). On the other hand, gas circulation, as opposed to mud circulation, eliminates the weight of the mud column bearing down

* Corresponding author.
E-mail address: jlucpl@jlu.edu.cn (P.-L. Cao).

https://doi.org/10.1016/j.petsci.2024.12.012
1995-8226/© 2024 The Authors. Publishing services by Elsevier B.V. on behalf of KeAi Communications Co. Ltd. This is an open access article under the CC BY-NC-ND license (http://creativecommons.org/licenses/by-nc-nd/4.0/).

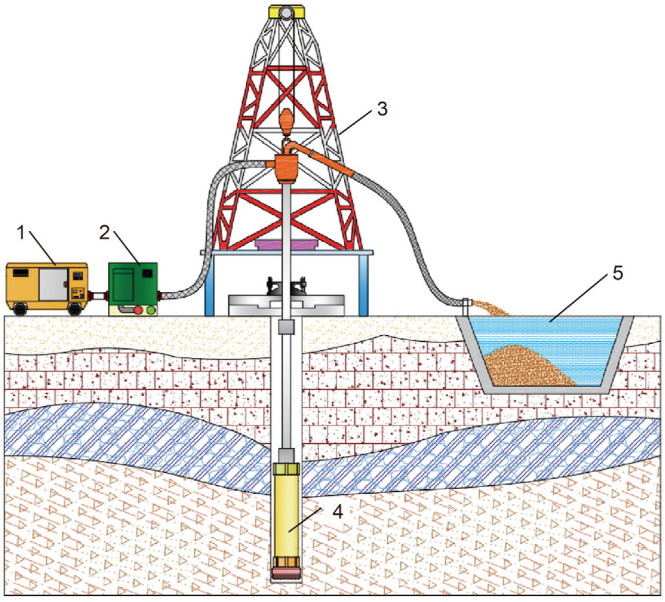

Fig. 1. Schematic diagram of the pneumatic hammer drilling process. 1-air compressor; 2-booster; 3-drill tower; 4-pneumatic DTH hammer; 5-grit reservoir.

on the formation, diminishing the chip hold-down effect and further enhancing ROP (Bui et al., 1997; Hu et al., 2015; He et al., 2018). For instance, the GQ-127c air DTH hammer reached penetration rates of up to 11.35 m/h at the Sichuan Copper Mine in China (Zhao et al., 2016). Therefore, the notably fast penetration rates of this technology in hard formations make it particularly attractive for directional drilling. However, the pneumatic hammer, originally designed for vertical drilling, to directional drilling faces challenges (Bui et al., 1997; Zhao et al., 2015). Specifically, in oblique sections, the non-rotational nature of the drill string requires the pneumatic hammer to rotate the drill bit to prevent repeated crushing and eventually form a round hole.

Two methods of pneumatic hammers used for directional drilling have been proposed. One combines a pneumatic hammer and a PDM, which rotates the entire hammer to break rock. Field testing of the motor was conducted in the Berea sandstone in Kentucky and Virginia, which demonstrated notable enhancements in drilling cycle and cost (Pletcher et al., 2010). However, most gas-driven PDMs are generally higher than the rotational speed range of 30–50 r/min required for pneumatic hammers, necessitating the further development of their low-speed capabilities (Hu et al., 2015). The other design of the pneumatic hammer incorporates both impact and rotary drill bit functions, known as self-rotating pneumatic hammer (Bui et al., 1997; He et al., 2011; Liu et al., 2015; Bo et al., 2022). This hammer is unique due to its built-in novel rotational bit-drive mechanism. During operation, the energy from high-pressure air is divided, with a portion dedicated to driving the piston for high-frequency impact drilling to fracture rocks, and another portion utilized for rotating the drill bit, cutting the rock ridges between impacts, and, consequently, eliminating the necessity to rotate the drill pipe. For instance, Bui et al. (1997) developed a novel pneumatic hammer with rotation function, named Steerable Percussion Air Drilling System (SPADS), and applied it alongside PDM for directional drilling in Greenville's granite formation, achieving penetration rate of up to 18 m/h, 12 times that of the PDM. This confirms the great potential of pneumatic hammers in directional wells. In addition, as weight-on-bit increases, the torque required to rotate the bit as well, the impact energy yielded by SPADS decreases rapidly. This phenomenon occurs because the torque required to effectively cut the rock ridges between impacts sacrifices the hammer's impact energy. The torque varies depending on different formation and weight-on-bit conditions, with the hammer's impact energy serving as the primary source of rock crushing. This emphasizes the necessity for the self-rotating pneumatic hammer to maintain sufficient impact energy for rock fragmentation while rotating the drill bit. To address this, a self-rotating pneumatic hammer performance method needs first to be developed, which clarifies the mechanism of piston motion and accurately evaluates impact and rotational performance values under various torques. However, research on self-rotating pneumatic hammers has primarily concentrated on examining the mechanical characteristics of their internal components (He et al., 2011; Liu et al., 2015; Bo et al., 2022).

Concerning the research on conventional pneumatic hammers, diverse approaches such as theoretical, simulation, and experimental research have been utilized. These can provide valuable insights for modeling the performance of the self-rotating pneumatic hammer. A mathematical model to study the regulation of piston movement, and assess the impact performance of the hammer is established in the study by Chiang and Stamm (1998). To enhance its calculated accuracy, the model was modified to determine the pressure of the gas by applying differential equations of energy conservation (Xiong et al., 2011; Zhao et al., 2015; Kim et al., 2019; Yin, 2020). However, the theory cannot be directly extrapolated to the self-rotating pneumatic hammer due to the presence of a built-in rotational mechanism, which significantly impacts the reciprocating motion of the piston.

Furthermore, Computational Fluid Dynamics (CFD) is also widely used in obtaining the output performance. Unlike mathematical models, which have limited insight into the dynamic response of airflow and piston within hammer, CFD stands out as a precise and efficient method capable of capturing internal details (Dixon and Partopour, 2020; Bournet and Rojano, 2022; Kong and Guan, 2023). Zhang et al. (2019) modeled the dynamic response of the gas and piston within the hammer using CFD and investigated the influences of piston mass, rebound coefficient, and inlet pressure on the impact performance yielded by hammer. On this basis, A deep study into the influence of air distribution and radial structural dimension values on impact performance was conducted in the work of Cao et al. (2023). Therefore, this approach can be applied to establish a numerical method for the self-rotating pneumatic hammer, elucidating the motion mechanism of the piston and investigating the effects of added structural parameters and drilling conditions on its output performance.

From the literature reviewed, research on the self-rotating pneumatic hammer is in the design phase, with few experiments and engineering applications to test their reliability. Furthermore, there is an absence of a method for evaluating the output performance of this hammer. Therefore, this study aims to propose a novel structure for self-rotating pneumatic hammer (NSH) and introduce its structure and working principle. CFD simulation is then employed to analyze the internal dynamic response of the airflow and piston to obtain output performance values. Meanwhile, a test bench is designed to record data concerning chamber pressure and piston displacement, as well as recording its operational status and rock fragmentation during drilling into granite. On this basis, how torque load, key parameters of the additional rotation mechanism, and well deviation angle influence impact and rotational performance are studied in detail, providing research for further early application of the self-rotating pneumatic hammer in directional well.

2. A novel normal circulation self-rotating pneumatic hammer (NSH)

2.1. Structure and working principle of the NSH

This study presents a novel self-rotating pneumatic hammer (NSH), which sacrifices the impact energy of the piston to rotate the drill bit and, consequently, eliminates the necessity to rotate the drill pipe. NSH consists of a connector, valve seat, upper and lower outer cylinder, piston, inner cylinder, anti-rotation sleeve, upper-rotation sleeve, lower-rotation sleeve, spacer bush, and drill bit, depicted in Fig. 2. It adds a built-in rotational mechanism (ii) to the conventional DTH hammer gas distribution assembly (i). Thus, its air distribution principle is similar to that of the conventional hammer and is yet unique because of its rotational bit-drive mechanism.

Specifically, the piston is axially extended with the addition of upper and lower rotation sleeves along the extension. Screw keys are evenly distributed on the outer diameter of the piston extension, which engages with screw groove tracks on the inner diameter of the upper-rotation sleeve. Interlocking wedge-shaped teeth are evenly distributed between the upper and lower rotation sleeves. As illustrated in Fig. 3(I-VI), when the piston moves upward axially, the friction between the screw keys and grooves drives the upper-rotation sleeve to rise, and then, it disengages from the lower-rotation sleeve. Notably, as the ascending upper-rotation sleeve reaches the step of the lower-outer cylinder, it ceases to ascend and rotates, defining the engagement distance of the rotation sleeves (denoted as L_{ed}) as the maximum distance it can ascend. Conversely, shown in Figs. 2 and 3(VII-XII), as the piston moves downward axially, the upper-rotation sleeve falls. Once it reaches L_{ed}, the key at its bottom, engaging with the one on the top of the lower rotation sleeve, drives the lower-rotation sleeve to rotate clockwise. The rotation of the lower-rotation sleeve is then transmitted to the drill bit by spline keys in such a manner that the drill bit rotation motion between impacts is realized. Thus, the piston accumulates energy during its upward movement, and upon descent, utilizes this energy to impact and rotate the drill bit. The drill bit operating condition is presented in Table 1. In addition, an anti-rotation sleeve is installed between the lower-outer cylinder and the piston, preventing the piston from rotating.

The air distribution mechanism of the NSH resembles that of a conventional hammer, featuring front and rear chambers, as shown in Fig. 3. The piston, powered by compressed air, also functions as a sliding valve, alternately directing high-pressure gas into the chambers. During the piston ascent phase, air enters the front chamber, propelling the piston up until the piston reaches L_{be}. In this process, the rear chamber connects to the downhole and exhausts its air. While for the front chamber, the air is intakes until the piston reaches L_{fi}. Both chambers close until piston reaches L_{bi}, compressed air quickly enters the rear chamber, causing the piston to decelerate. When the piston runs to L_{fe}, the front chamber exhausts its air rapidly. The piston decelerates, and comes to a stop, and the distance ascended by it is termed the maximum piston displacement. The piston ascent phase is referred to as the return phase, at which point the phase ends and the piston begins to move downward. In this phase, chambers undergo opposite air intake and exhaust processes, respectively, as depicted in Fig. 3. The piston is propelled downward by its gravitational potential energy and rear chamber pressure energy. These air distributions, combined with the drill bit operation, define twelve distinct stages, as presented in Table 1.

2.2. Evaluation index

The proposed NSH changes the working mode of conventional hammers by incorporating a unique rotation mechanism. This mechanism sacrifices the piston's impact energy to enable the hammer to function as both an impact and rotary drill bit. The working mode introduces new evaluation indexes, i.e., the single rotational angle of the drill bit and rotational speed. Correspondingly, impact indexes still encompass impact velocity and frequency (Cao et al., 2024). Additionally, pressure drop is a key parameter in air compressor selection, making it an essential index.

The single rotational angle of the drill bit can be calculated as:

$$\beta = \frac{L_p - L_{ed}}{G} \cdot 360 \tag{1}$$

where, G represents the pitch of the screw groove on the upper-rotation sleeve, mm.

The rotational speed n (r/min) can be expressed as,

$$n = \frac{\beta F}{6} \tag{2}$$

where, F represents the impact frequency of the NSH, Hz.

3. Laboratory testing

In this study, a test bench was built to record impact and rotational performance values of NSH output across various variables, including mass-flow rate, output torque, and well deviation angle, as well as to assess the ability of NSH to drill into granite without rotating the drill pipe, as shown in Fig. 4. The bench consists of air compressor, experimental bench, Φ127NSH for testing, vortex flow sensor, pressure sensor, torque sensor, high-speed camera, and winch.

Based on the working principle in Section 2.1, an NSH with an outer diameter of 127 mm was developed, depicted in Fig. 4(c). The essential parameters of the air distribution mechanism and radial structural dimensions of this Φ127NSH are detailed in Table 2.

In the performance testing experiments of the NSH, to record its impact performance at different output torques, the torque load transfer mechanism and its collection assembly were added to simulate the torque exerted on the drill bit by the formation, as shown in Fig. 4(d). The torque load is applied to the brake disk by

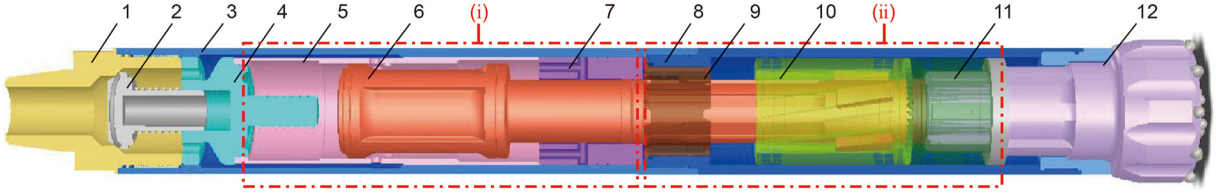

Fig. 2. 3D schematic of the NSH structure. 1-upper connector; 2-non-return valve; 3-upper-outer cylinder; 4-valve seat; 5-inner cylinder; 6-self-rotating piston; 7-spacer bush; 8-lower-outer cylinder; 9-anti-rotation sleeve; 10-upper rotation sleeve; 11-lower rotation sleeve; 12-drill bit; (i)-Valve assembly; (ii)-Rotary assembly.

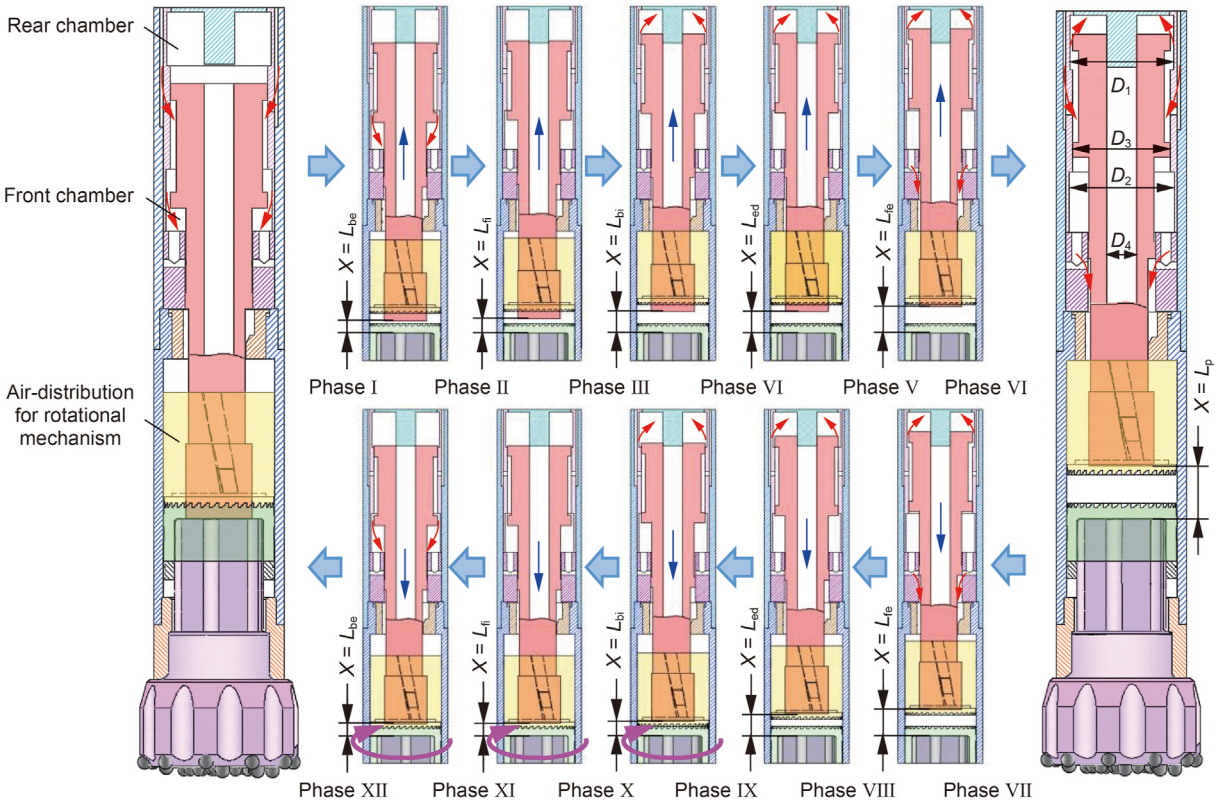

Fig. 3. Status of piston, upper and lower rotation sleeve, drill bit, as well as airflow in a single cycle. The red arrow denotes the airflow direction, the pink and blue arrows denote the direction of drill rotation and piston movement, respectively.

Table 1
Piston position, air chamber stages, and drill bit operating condition.

	Phase	Piston displacement X	Front chamber condition	Rear chamber condition	Drill bit operating condition
Return stroke	I	$0 \le X < L_{be}$	Air intake	Air exhaust	Non-rotating drill bit
	II	$L_{be} \le X < L_{fi}$		Closed-compressed	
	III	$L_{fi} \le X < L_{bi}$	Closed-expanded		
	IV	$L_{bi} \le X < L_{ed}$		Air intake	
	V	$L_{ed} \le X < L_{fe}$			
	VI	$L_{fe} \le X < L_p$	Air exhaust		
Impact stroke	VII				
	VIII	$L_{ed} \le X < L_{fe}$	Closed-compressed		
	IX	$L_{bi} \le X < L_{ed}$			Rotating drill bit
	X	$L_{fi} \le X < L_{bi}$		Closed-expanded	
	XI	$L_{be} \le X < L_{fi}$	Air intake		
	XII	$0 \le X < L_{be}$		Air exhaust	

using DBF-L10 pneumatic brake, which is then transferred to NSH through the driven wheel and the main wheel with plane bearing. The TH4803A dynamic torque sensor, with a measurement range of 0–1000 N·m and speed range of 0–1000 r/min, is mounted on the driven wheel to record the applied torque load. An extension rod, on the other hand, relies on threads to connect to the piston and extends to the NSH outside, seen in Fig. 4(c). This way, the piston movement can be obtained by recording the movement of the one-piece extension rod using an AE-110 high-speed camera (frame rate of 1000 fps, resolution of 1280 × 860). A hollow rigid anvil instead of drill bit for better torque application and to allow smooth axial movement of the extension rod, as shown in Fig. 4(e). The shanks of the hollow hard anvil and the drill bit have the same structure, dimensions, and materials, therefore do not influence the initial position of the piston movement inside the NSH and the value of the rebound coefficient. The hollow anvil has a vertical channel in the center to allow smooth axial movement of the extension rod, and the bottom of the hollow anvil transmits and measures the NSH torque output through a flat key. Furthermore, an electric winch adjusts the tilt of the NSH.

Additionally, An AE-S piezoresistive high-frequency pressure sensor (range of 0–1.5 MPa, accuracy of 0.5% FS) and a LUGB-DN80 vortex street flow sensor (range of 0–15 m^3/min, accuracy of 1% FS) are employed to measure the pressure and volume flow rate of the gas at the NSH inlet, respectively. The pressure sensor is also utilized to measure the gas pressure inside the chambers. Considering the chamber sealing within the NSH, improvements were made, and the relevant details are shown in Fig. 4(f). For rear chamber, a through-hole was drilled along the inlet of the valve seat, into which an 'L'-shaped connecting tube was inserted. A hole was then

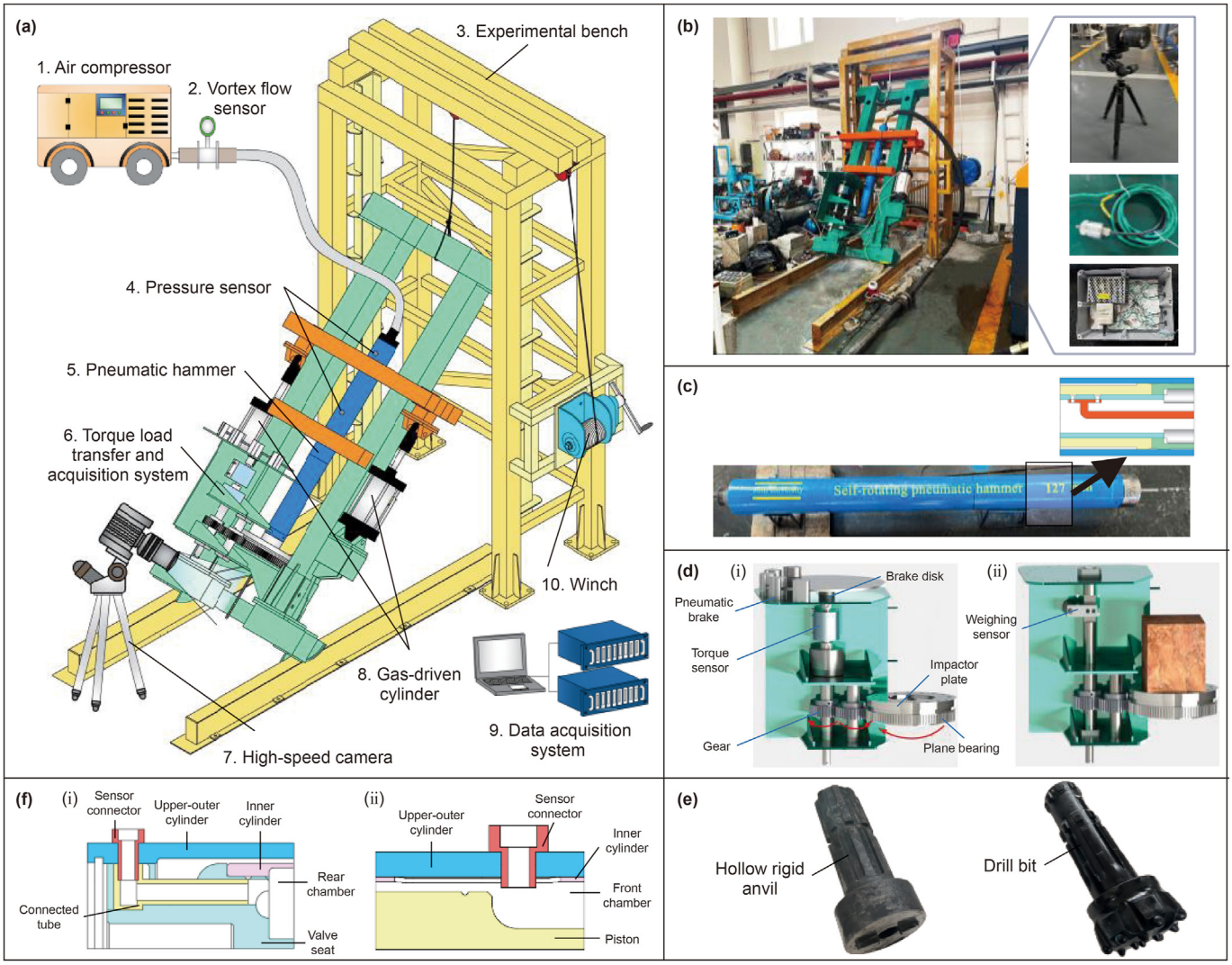

Fig. 4. NSH output performance and drilling capability test bench. (**a**) schema, (**b**) real picture of test bench, (**c**) real picture of Φ127NSH post-machining, (**d**) torque load transfer mechanism and its collection assembly, (**e**) hollow rigid anvil and drill bit, and (**f**) installation details of the pressure sensor in the front and rear chambers.

Table 2
Structural parameters and piston mass values for Φ127NSH.

L_{be}, mm	L_{fi}, mm	L_{bi}, mm	L_{fe}, mm	L_s, mm	D_1, mm	D_2, mm	D_3, mm	D_4, mm	G, mm	L_{ed}, mm	m, kg
38	45	67	81	140	104	104	34	94	1750	40	22

drilled at the corresponding location on the upper-outer cylinder. The sensor connector was then threaded onto the 'L'-shaped connection tube, and the pressure sensor was threaded onto the sensor connector. For the front chamber, installation holes were set in the corresponding positions of the inner cylinder and upper-outer cylinder. The sensor connector was threaded into these holes, followed by the threading of the pressure sensor onto the sensor connector. This design ensures the effective transmission of pressure measurement signal from the front chamber to the measuring card.

In the experiment assessing the NSH's drilling ability on granite without rotating the drill pipe, a Φ138 mm drill bit replaced the hollow rigid anvil. A granite sample measuring 300 × 300 × 200 mm was placed under the NSH and secured with a threaded rod to ensure synchronous rotation with a flat bearing, as depicted in Fig. 4(d(ii)). A weighing sensor replaced the torque sensor. During NSH operation, the rock tended to rotate in the same direction due to the frictional force and torque exerted by the drill bit. At this point, the force end of the weighing sensor mounted on the drive shaft pressed against the bracket mounting plate, limiting the rotation of the drive system and outputting the torque value required to break the rock by the NSH. Additionally, gas-driven cylinders 7 installed on both sides of the sliding frame applied weight-on-bit to the NSH, facilitating feed motion.

Three sets of performance evaluations were conducted for the Φ127NSH, followed by tests to assess its capability in drilling through granite, and Table 3 lists specific mass-flow rates, deviation angles, and torque loads main testing parameters. It is held on the experimental bed utilizing clamps, the torque load is applied by adjusting the pneumatic brake, and the tilt angle of NSH is set by

Table 3
Air, deviation angle, and load torque values.

		Mass rate M, kg/s	Deviation angle θ, °	Torque load T, N·m	Engagement distance in rotary sleeves L_{ed}, mm
Experiment	#1	0.06	0, 15, 30, 45,60,	100	40
	#2	0.18	75, 90		
	#3		0	0, 32, 100, 330	
Simulation	#1	0.06	0, 15, 30, 45,60,	100	
	#2	0.18	75, 90		
	#3		0	0, 32, 100, 200, 300, 330, 400	
	#4			300	10, 25, 40, 55, 70, 85

adjusting an electric winch. The sensors and air compressor are then activated.

Fig. 5(a) illustrates the curves of the mass-flow rate at the NSH inlet and the pressure within its rear chamber. Both parameters remain stable initially, then gradually increase during the developmental stage, and finally stabilize. Specifically, the pressure stabilized at around 10 s, followed by the mass-flow rate, which stabilized at around 12.2 s, reaching a value of 0.06 kg/s. This phase signifies the transition of Φ127NSH into a stable impact stage. At this point, the movement of the extension rod would be recorded using the camera, as shown in Fig. 5(b). Piston's real-time displacement is tracked through the bottom notch. This enables derivation of the impact frequency F, impact velocity U_p, and maximum piston displacement L_p from the data of piston displacement.

4. Numerical method for Φ127NSH

4.1. Computational domain and grid independence

ANSYS FLUENT is utilized to simulate the dynamic response of airflow and piston during the operation of Φ127NSH. The computational domains for simulation, extracted from the hammer, encompass the front and rear chamber, inlet and outlet ports, as well as air-distribution chamber of the rotation mechanism, as shown in Fig. 6. Dimensional specifics are outlined in Table 2. To satisfy the continuity equation iteration requirements, a clearance of 0.1 mm is kept between the inner cylinder and the piston (Cao et al., 2023). This domain is divided into hexahedral meshes.

A grid-independent analysis was performed, to balance a balance between accuracy and cost in evaluating the results of the

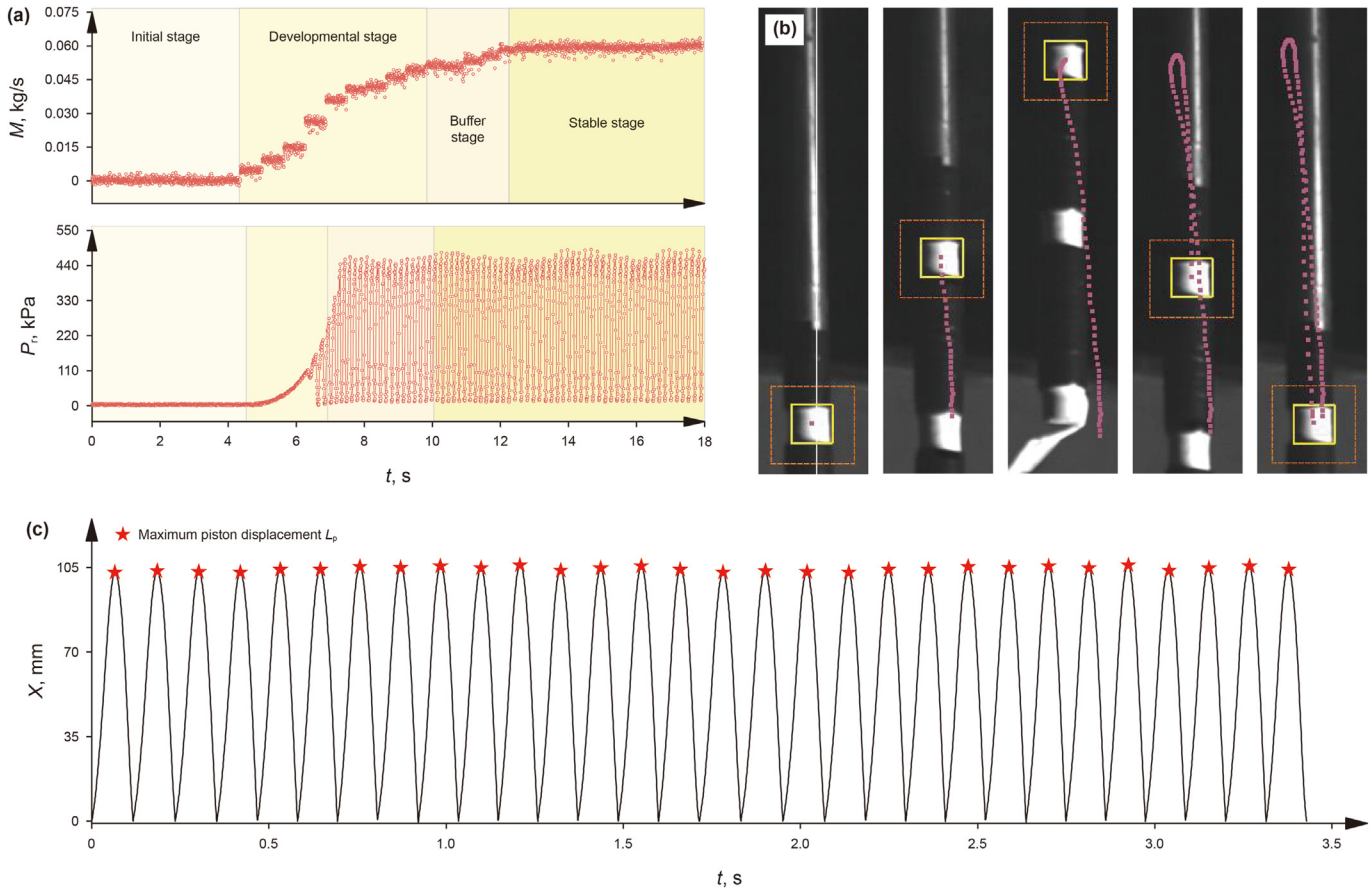

Fig. 5. (**a**) Mass-flow rate at the NSH inlet and pressure within its rear chamber vs. time curve, (**b**) extension rod motion video, and (**c**) piston displacement (#1, $\theta = 0°$).

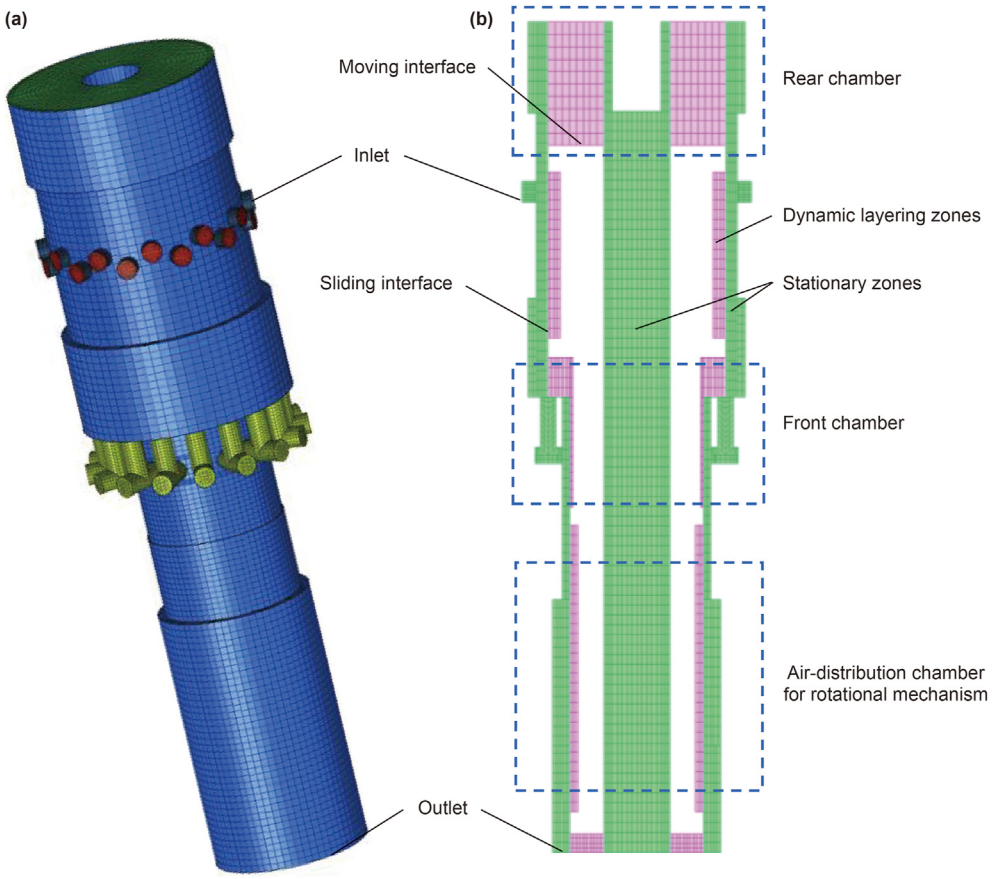

Fig. 6. 3D and semi-profile schematic of the generated Φ127NSH computational domain mesh with boundary conditions.

NSH. This analysis involved varying grid numbers, as detailed in Table 4, with the grid independence criterion set at a rate of change in results of less than 5% (Wang et al., 2014). Consequently, a grid number of 0.6 million was chosen, meeting this criterion.

4.2. Materials and turbulence governing equations

Two materials were considered in the numerical model: air and steel. Air is treated as an ideal-gas, while the steel piston is set as a rigid body with uniform density. Airflow within the domain is modeled using Reynolds-averaged Navier-Stokes (RANS) equations, which in general forms can be described as:

Continuity equation,

$$\frac{\partial \rho_a}{\partial t} + \nabla \cdot (\rho_a \boldsymbol{v}) = 0 \tag{3}$$

Momentum equation,

$$\frac{\partial}{\partial t}(\rho_a \boldsymbol{v}) + \nabla \cdot (\rho_a \boldsymbol{v}\boldsymbol{v}) = -\nabla P + \nabla \cdot (\boldsymbol{\tau}) + \rho_a g \tag{4}$$

$$\boldsymbol{\tau} = \mu \left[\left(\nabla \boldsymbol{v} + \nabla \boldsymbol{v}^T \right) - \frac{2}{3} \nabla \cdot \boldsymbol{v} I \right] \tag{5}$$

where ρ_a stands for the gas density, $\boldsymbol{\tau}$ stands for the stress tensor, P represents the static pressure, I represents the unit tensor, t represents the time variable, $\boldsymbol{v}$ stands for the mean velocity, $\rho_a g$ represents the gravitational body force, T is air temperature, and μ represents the molecular viscosity.

Energy equation,

$$\frac{\partial}{\partial t}\left[\rho_a \left(e + \frac{1}{2}\boldsymbol{v}^2\right)\right] + \nabla \cdot \left[\rho_a \boldsymbol{v}\left(h + \frac{1}{2}\boldsymbol{v}^2\right)\right] = \nabla \cdot (K \nabla T) + \nabla \cdot (-P\boldsymbol{v} + \boldsymbol{\tau} \cdot \boldsymbol{v}) + \boldsymbol{v} \cdot \rho_a g \tag{6}$$

where e stands for gas internal energy per unit mass, h is enthalpy,

Table 4
Effect of grid numbers on the performance of numerical models.

Number of grid elements, million	Impact velocity U_p, m/s	Impact frequency F, Hz	Pressure drop ΔP, kPa	Computation time t_1, h
0.2	4.93	12.1	880	11.5
0.4	4.76	12.3	890	38.5
0.6	4.81	12.8	860	60.5
0.8	4.80	12.8	870	92
1.0	4.81	12.7	870	114

and K is thermal conductivity.

Furthermore, the ideal gas state equation is included.

$$\rho_a = \frac{P_{op} + P}{\frac{R}{M_w} T} \tag{7}$$

where M_w represents the molecular weight, R represents the universal gas constant, and P_{op} is the operating pressure.

The gas flows inside the NSH can reach high Reynolds numbers, resulting in turbulent flow. Consequently, to accurately model this turbulent flow, the RNG k-ε turbulent method is chosen for solving the RANS equations, considering its proven robustness, efficiency, and accuracy in addressing turbulent flow problems (Yakhot et al., 1992; Zhang et al., 2007). The scalable wall function is used. Details of transport equations are outlined below,

$$\frac{\partial}{\partial t}(\rho_a k) + \frac{\partial(\rho_a k v_i)}{\partial x_i} = \frac{\partial}{\partial x_i}\left(\alpha_k \mu_{eff} \frac{\partial k}{\partial x_j}\right) + G_k + G_b - \rho_a \varepsilon - Y_M \tag{8}$$

$$\frac{\partial}{\partial t}(\rho_a \varepsilon) + \frac{\partial(\rho_a \varepsilon v_i)}{\partial x_i} = \frac{\partial}{\partial x_j}\left(\alpha_\varepsilon \mu_{eff} \frac{\partial \varepsilon}{\partial x_j}\right) + G_{1\varepsilon}\frac{\varepsilon}{k}(G_k + G_{3\varepsilon} G_b) - C_{2\varepsilon}\rho_a \frac{\varepsilon^2}{k} - R_\varepsilon \tag{9}$$

$$\mu_t = \rho_a C_\mu \frac{k^2}{\varepsilon} \tag{10}$$

within the equation, ε is the rate of dissipation, Y_M indicates the contribution of fluctuating dilatation in compressible turbulence to the overall dissipation rate, k represents the turbulent kinetic energy. μ_{eff} stands for the effective viscosity of the gas. G_k and G_b signify the generation of turbulence kinetic energy due to mean velocity gradients and buoyancy, respectively. Additionally, α_k and α_ε are the inverse effective Prandtl numbers for k and ε, respectively, and $C_{1\varepsilon}$ $C_{2\varepsilon}$ and $C_{3\varepsilon}$ are constants. Turbulence eddy viscosity is denoted by μ_t, with C_μ being a constant set at 0.0845 (Yakhot et al., 1992; ANSYS Inc, 2020).

4.3. Mesh update strategy and user-defined functions (UDFs)

Dynamic Layering (DL) technique is utilized to calculate the values of fluid domain parameters with time-varying geometries, suitable for hexahedral/prismatic/quadrilateral mesh, with the requirement of having a one-sided boundary for the moving face (ANSYS Inc, 2020; Li et al., 2021b). Therefore, it is utilized to update the mesh surrounding the moving surfaces, which varies due to the axial motion of the piston within the NSH. Specifically, as shown in Fig. 6(b), the computational domain around the piston is divided into dynamic layering and stationary zones, with the interface set between the two zones, ensuring the moving boundary is one-sided. During the piston movement, if the height of the grid layer adjacent to the piston's face exceeds a set threshold, this grid layer will split into two layers. Conversely, if the height of the grid layer falls below the threshold, the two grid layers adjacent to the face will merge into a single layer, facilitating the mesh updating process (Gao et al., 2019).

DEFINE_CG_MOTIONH macro in UDFs is utilized to specify the piston movement inside the Φ127NSH. The piston velocity needs to be defined and then transmitted to Fluent. F_P is used to acquire the pressure from the simulation, which is then passed to the UDFs. To specify the piston's velocity, the forces exerted on the tilted piston during the return stroke were analyzed, as shown in Fig. 7, including air pressure, friction force between the piston and the inner cylinder F_{cf}, and gravitational component force. The force balance equation, as given by Newton's second law, is,

$$ma = P_f A_{pf} - P_r A_{pr} + P_c A_p - mg\cos\theta - f_c mg \sin\theta \tag{11}$$

where m stands for the piston mass, a is the acceleration of the piston, P_f, P_r, and P_c are the gas pressures in the front chamber, rear chamber, and bottom-hole, respectively. A_{pf}, A_{pr}, and A_p are the corresponding piston areas. θ is the deviation angle of the well, and f_c represents the coefficient of friction.

During the stroke stage, when the piston moves downward without drill bit rotation, the force balance equation, as given by Newton's second law, is,

$$ma = P_f A_{pf} - P_r A_{pr} + P_c A_p - mg\cos\theta + f_c mg \sin\theta \tag{12}$$

When the piston pushes the drill bit to rotate via the rotating mechanism, it must counter the resistance posed by the formation. In practical operations, if the torque exerted on the drill bit by the formation is denoted as M_T, and the resistance F_T experienced by the rotating mechanism can be computed as:

$$F_T = \frac{2M_T}{d_T} \tag{13}$$

The force encountered by the piston undergoes dynamic changes as a result of the dynamic pressure variations in front and rear chambers and is influenced by various factors, helix angle α of the key, deviation angle θ, friction coefficient f_c, and the resistance F_T of the rotational mechanism. The forces acting on the upper-rotation sleeve and the piston helical key during operation are displayed in Fig. 7.

The upper-rotation sleeve is subjected to the support force F_N and the friction force F_f exerted on it by the piston, to overcome the resistance F_T exerted by the formation:

$$F_T = F_{T2} - F_{T1} = F_N \sin\alpha - F_{cf}\cos\alpha \tag{14}$$

Thus, the force axially on the piston during impact stoke, is,

$$\begin{aligned} ma &= F_P - mg\cos\theta + \mu mg\sin\theta + F_{a1} + F_{a2} \\ &= P_f A_{pf} - P_r A_{pr} + P_c A_p - mg\cos\theta + \mu mg\sin\theta + F_N\cos\alpha \\ &\quad + F_{cf}\sin\alpha \end{aligned} \tag{15}$$

Given the coefficient of friction f_c for the material, the relationship between frictional force and supporting force is as follows:

$$F_f = \mu F_N \tag{16}$$

Further, the force exerted on the piston can be expressed by substituting Eqs. (13), (14) and (16) into Eq. (15) for solution.

$$ma = F_{pf}A_{pf} - F_{pr}A_{pr} + F_{pc}A_p + \frac{\cos\alpha + \mu\sin\alpha}{\sin\alpha - \mu\cos\alpha}\frac{2M_T}{d_T} - mg\cos\theta + f_c mg\sin\theta \tag{17}$$

When the time step is sufficiently small, the acceleration of the piston can be considered constant within each time step. Consequently, the velocity U_i and displacement X_i of the piston during the ith time step can be expressed as follows,

$$U_i = U_{i-1} + a_i \Delta t \tag{18}$$

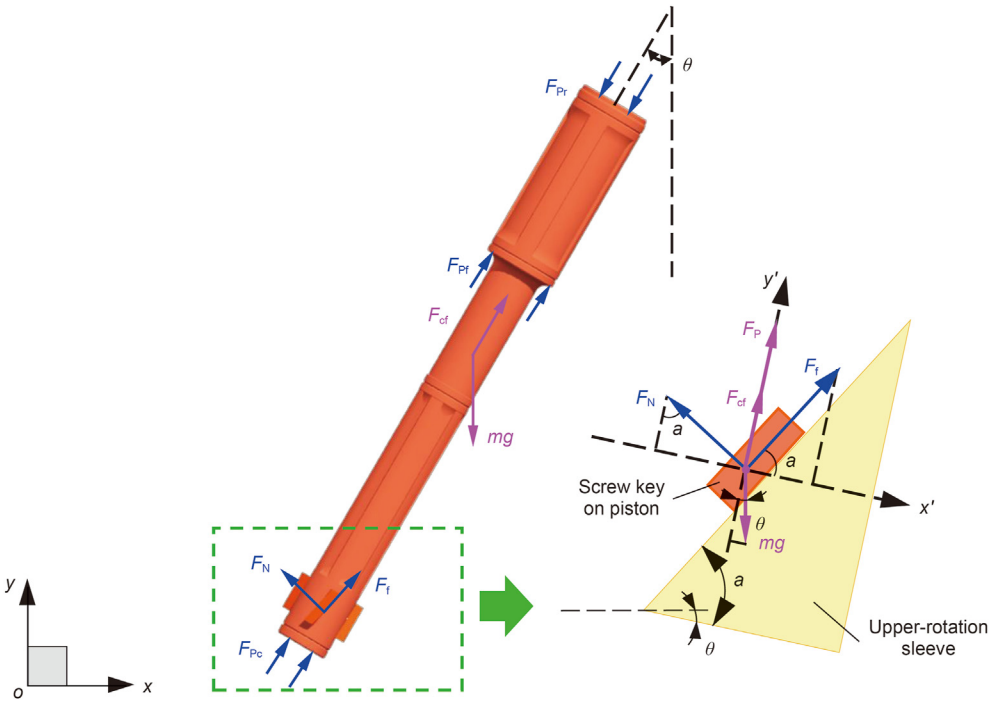

Fig. 7. Diagram of the force on the piston in the inclined state.

$$X_i = X_{i-1} + U_{i-1}\Delta t + \frac{1}{2}a_i\Delta t^2 \tag{19}$$

The piston hits the bit at the end of its impact stroke and, then, gains upward rebound velocity into the next cycle. The upward rebound velocity can be calculated by:

$$U_i = -EU_P \tag{20}$$

where E stands for the restitution coefficient, and U_p represents the piston's final velocity as it hits the drill bit.

4.4. Simulation program

The mass-flow inlet is utilized as the inlet condition, while pressure-outlet as the outlet condition with the value of the back-pressure. The temperature of the gas at the port was maintained as 293 K. The wall boundaries were defined as adiabatic and no-slip. The governing equations were discretized using the finite volume method, employing the pressure-based Coupled solver algorithm to ensure coupling between pressure and velocity fields. Additionally, a second-order windward discretization scheme was implemented to enhance accuracy. In the simulation, the timestep size was set to 1E-4 s to avoid negative volume resulting from piston displacement exceeding the mesh height within a single timestep. To ensure convergence, a maximum of 200 iterations per timestep were allowed.

5. Results and discussion

Experimental and simulated performance metrics of the designed Φ127NSH (including maximum piston displacement L_p, impact frequency F, impact velocity U_p, single rotational angle of the drill bit β and rotational speed n as a result of changes in different mass-flow rate M, well deviation angle θ, and torque load T) and the pressure inside each chamber are compared, followed by analyzing the ability of the Φ127NSH to drill on granite without rotating the drill pipe. Following this assessment, a mechanism of piston motion was provided, along with an investigation into the influence of torque load, engagement distance of the rotation sleeves, and deviation angle on both impact and rotational performance of the hammer.

5.1. Validation of the numerical model

Fig. 8 displays the performance metrics, (i.e., U_p, F, ΔP), of Φ127NSH under Group #1, #2, and #3, both in simulation and experiment. The fifth-cycle data from the simulation were utilized for the study, prompted by the presence of a rebound effect E. The piston's rebound causes fluctuations in U_p during the initial cycles until the disparity in U_p values between the fifth and sixth cycles is less than 5%. In Group #1, both the impact velocity U_p and impact frequency F exhibited a negative correlation with well deviation angle θ in the experiment and simulation under a torque load T of 100 N·m and inlet-mass-flow M of 0.06 kg/s. As the value of θ increases from 0° to 90°, U_p and F in the experiment decreased from 2.33 to 1.92 m/s and 8.72 to 7.62 Hz, with decreases of 17.6% and 12.6%, respectively. Correspondingly, those in the simulation decreased from 2.2 to 2.08 m/s and 8.46 to 8.08 Hz. On the contrary, maximum piston displacement L_p is positively correlated with θ in the experiment increased from 92.45 to 103.02 mm, while in the simulation from 95.05 to 103.71 mm.

When the M raised to 0.18 kg/s, both the U_p and F in the experiment exhibited a significant increase, rising from 1.92 to 4.73 m/s and 7.62–12.63 Hz, respectively. Similarly, those in the simulation increased sharply from 2.08 to 4.81 m/s and 8.08–12.8 Hz, respectively. In Group #2, at a constant M of 0.18 kg/s, as θ increases from 0° to 90°, the experimental and simulated U_p exhibits slight variations around 4.81 and 4.72 m/s, respectively. F still shows a negative correlation with θ, and decreases from 12.62 to 12.2 Hz in the experiment, and 12.80 to 12.58 Hz in the simulation. Conversely, L_p displays a positive relationship with θ, in the

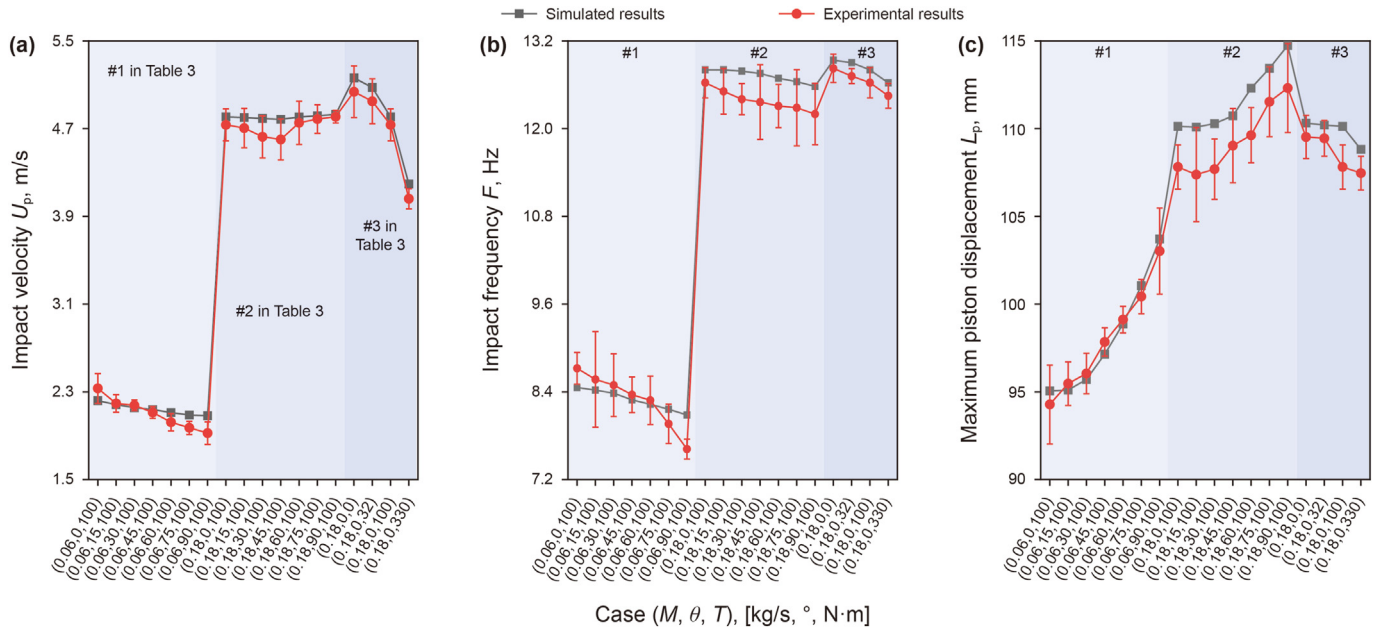

Fig. 8. Comparison of parameter values between experiment and simulation, (**a**) impact velocity, (**b**) impact frequency, and (**c**) maximum piston displacement (#1, #2, and #3 in Table 3).

experiment increased from 107.81 to 112.31 mm, while in the simulation from 110.13 to 114.74 mm. In Group #3, all the performance metrics, i.e., U_p, F, and L_p, exhibited negative correlations with T. As T increased from 0 to 330 N·m, U_p dropped from 5.04 to 4.06 m/s, F decreased from 12.82 to 12.45 Hz, and L_p decreased from 109.53 to 107.47 mm in the experiment. Similarly, in the simulation, U_p decreased from 5.16 to 4.19 m/s, F decreased from 12.94 to 12.63 Hz, and L_p decreased from 110.32 to 108.82 mm. The results showed that the maximum error between simulated and experimental data is 8.2%.

Fig. 9 shows the variations in air pressure within the chambers over multi-cycles, observed in simulation and experiment data, under consistent conditions of the torque load of 100 N·m, inlet-mass-flow of 0.18 kg/s, and well deviation angle of 0° (Group #2, $\theta = 0°$). The experimental and simulated pressure values within the chambers exhibit similar trends. Quantitatively, the peak pressures recorded during experimentation were 780.1 and 823.8 kPa for the front and rear chambers, respectively, compared to 796.2 and 859.7 kPa in the simulation, with errors of 2% and 4.4%, respectively. Cycle times derived from pressure curves were 82.98 and 78.4 ms for experiment and simulation, respectively, with an error of 5.52%. This discrepancy results in a deviation of 0.4 cycles as the cycle count extends to 8. Similar values and trends were demonstrated between the experimental and simulated pressure values within the gas chamber, further supporting that the simulation scheme of this study is applicable and reliable for studying the gas flow and piston behavior inside the NSH.

It is noteworthy that one potential reason for the error between simulation and experimental results could be the accuracy of the machining process. The fluid domain model is simplified, including

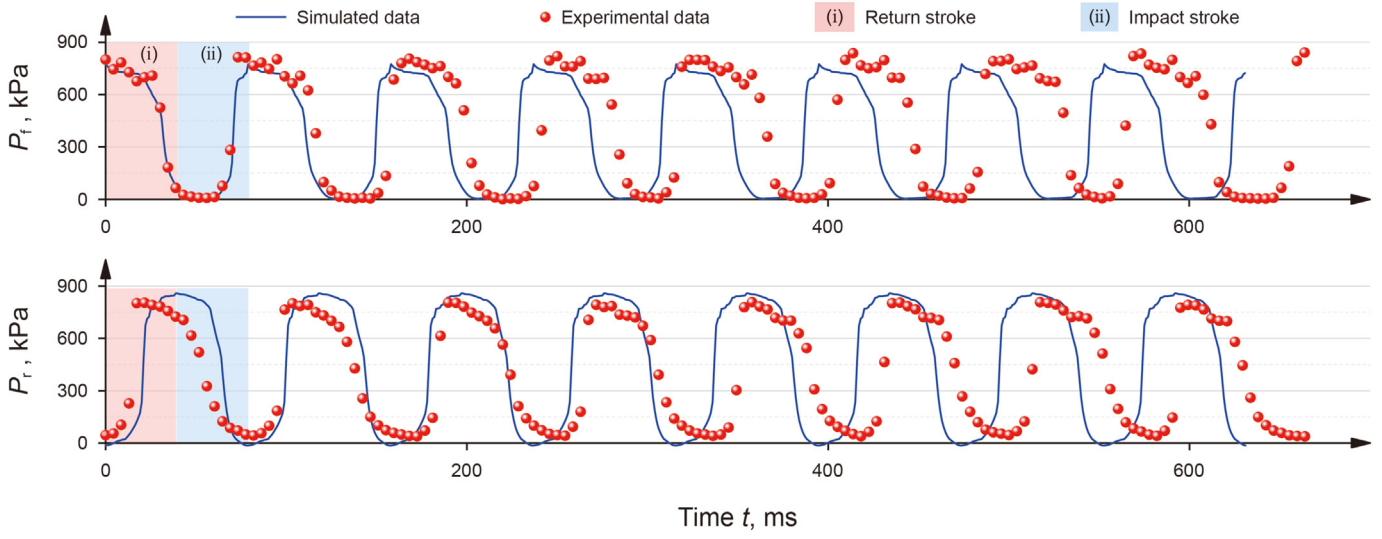

Fig. 9. Pressure in the front and rear chamber vs. time profiles between simulations and experiments.

neglecting geometric features such as chamfers, fillets, and heat transfer effects. Additionally, the operational characteristics of the NSH (high-frequency and high-energy impact of the piston on the anvil seat) may also contribute to this error. Specifically, stress generated during impact may propagate along the extension rod, inducing vibrations at its free end and thereby introducing errors in data collection. As a result, there is a discrepancy between the simulated and experimental results in Fig. 8, with the experimental data in Fig. 9 lags the simulated data.

5.2. Capacity of Φ127NSH crushing granite

To reduce the risk of excessive impact force generated by Φ127NSH causing direct fracturing of the granite, the experiment employed an airflow rate ranging from 2 to 5 m^3/min. The operational status of the Φ127NSH during the drilling process into granite samples measuring 300 × 300 × 200 mm is shown in Fig. 10(a). It is shown that Φ127NSH has successfully sacrificed its impact energy to rotate the drill bit and, consequently, eliminated the necessity of rotating the drill pipe and hammer, ultimately enabling drilling granite.

To analyze the developmental stages of rock fragmentation during the initial drilling phase, the rock surface was painted blue to distinguish the fragmentation zones. These zones were then extracted and post-processed to a yellow hue to differentiate them from the white background, as illustrated in Fig. 10(b). Observations indicate that complete shear crushing zones have formed in the 1st and 2nd circles (labeled i and ii) of the granite surface, while the 3rd circle (iii) has just begun to be crushed. This crushing sequence is attributed to the convex bottom design of the drill bit used, which allows gradual contact of the internal spherical teeth with the rock surface, progressing from the inside out. By intercepting the adjacent crushed zones within the 2nd and 3rd circles, distinct evidence of crushed and shear trajectory is evident in the 3rd circle. In contrast, the 2nd circle exhibits deeper pits, with continual development of crushed zones, resulting in a larger area of crushing. Quantitative comparisons show that the equivalent area of the crushing zone of a single spherical tooth in the deeper 2nd circle is about 2.6 times that of the 3rd circle. Therefore, the Φ127NSH successfully realizes both the functions of impact and rotary drill bit.

As the operating time of the Φ127NSH increases, boreholes gradually form on the rock surface, as displayed in Fig. 11. To clearly show the details of the crushed zone in the borehole, a fill light was used, resulting in a color difference between Figs. 10 and 11. These boreholes exhibit a stepped distribution at their bottoms, determined by the arrangement of the drill bit's edge and face teeth. In the crushed zone formed by the face teeth, the impact of the drill bit on the rock results in the formation of shallow-colored crushed pits, along with continuous shear rock zones between adjacent pits. Beyond this area lies the zone of crushed rock by the edge teeth, where the larger size of the edge teeth leads to a slightly larger single-circle rock crushed area compared to the face teeth. Additionally, the drill bit's edge teeth, while impacting and crushing rock, contribute to refining the borehole wall through shearing and grinding. Detailed images reveal a smooth and relatively even borehole wall surface created by the Φ127NSH, with no discernible areas of rock fracture or crushed pits.

5.3. Mechanism of the piston movement

The movement process of the piston within the Φ127NSH involves complex flow-structure interactions. Gas pressure within the chamber propels the piston axially, while its axial movement controls the opening and closing of the chamber's intake and exhaust ports, thus affecting the gas pressure. Additionally, a unique built-in rotational mechanism adds extra resistance against the piston's descent. To explain the motion mechanism of the piston, pressure variations in the chambers, and velocity and acceleration of the piston during a single cycle, were simulated (Fig. 12(a)). Further, the pressure contour and the piston's position at critical moments are displayed in Fig. 12(c).

At the outset, the front chamber connects to the NSH's intake, filling with high-pressure air to an internal pressure of about 775 kPa. Simultaneously, the rear chamber connects to downhole, maintaining internal pressure at a backpressure level. The pressure differential between the chambers pushes the piston upward. Subsequently, the front chamber undergoes sequential closure and exhaust, with the internal pressure gradually reducing to backpressure. This process is facilitated by the rising piston, which mechanically closes the intake and opens the exhaust ports. Meanwhile, the rear chamber experiences sequential closure and intake, gradually increasing the internal pressure to a peak of 859.7 kPa. The resulting opposing pressure differential drives the piston through an initial acceleration followed by deceleration, ultimately halting at a displacement of 108.93 mm. As the chambers undergo reverse conditions to those of the return stroke phase, the piston undergoes a similar acceleration followed by deceleration, finally hitting the bit at 4.74 m/s, completing a single impact.

It's worth noting that the area of the piston exposed to the front chamber (A_{pf}) is smaller than that in the rear chamber (A_{pr}), depicted in Fig. 12(b), where A_{pf} is 3.72E-3 mm^2, smaller than A_{pr}'s 6.03E-3 mm^2. Consequently, under same chamber pressure, the rear chamber exerts a greater force on the piston than the front

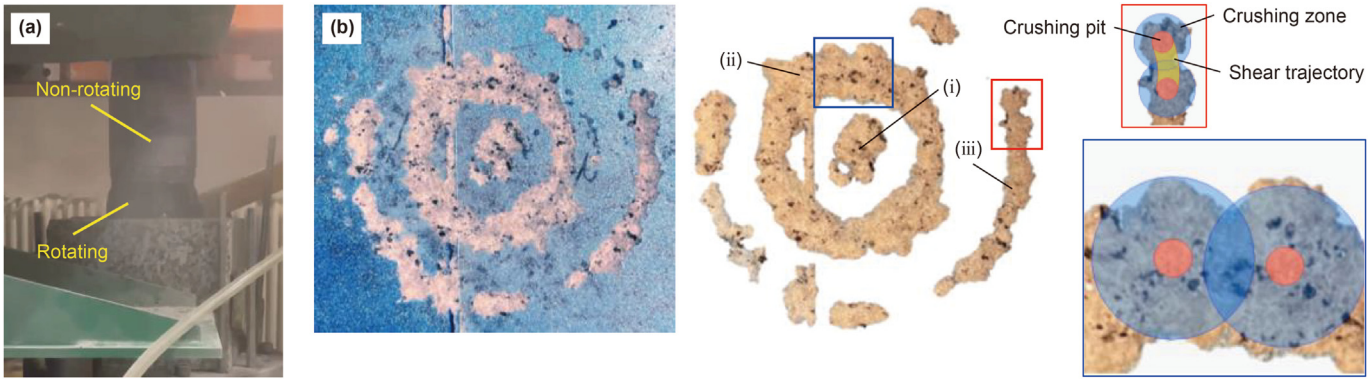

Fig. 10. (**a**) Φ127NSH working condition and (**b**) rock crushing condition.

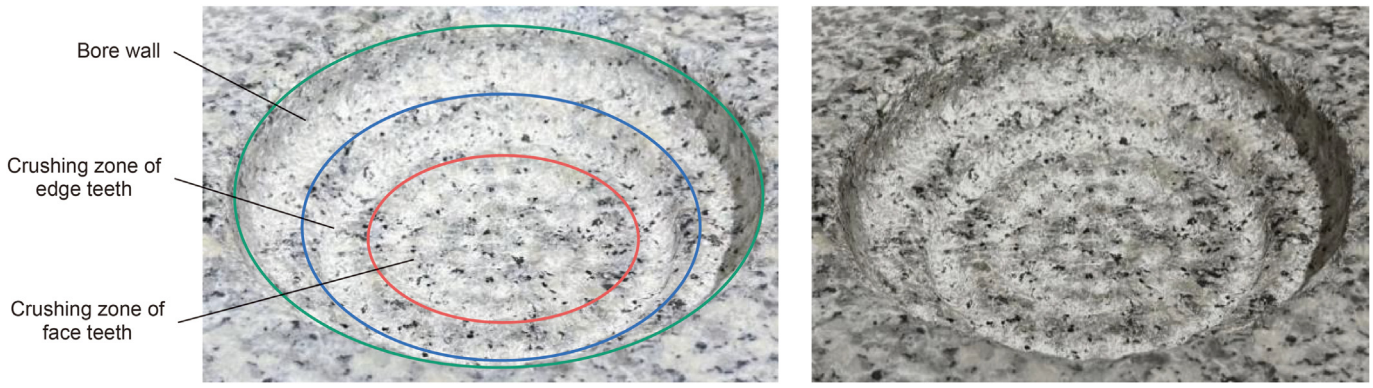

Fig. 11. Broken rock hole status.

chamber. The acceleration curve reveals a peak acceleration of 109.5 m/s^2, with a trough value of −250.6 m/s^2. Thus, the Φ127NSH is designed to rotate the drill bit during the impact stroke to minimize the effect on piston's acceleration compared to the return stroke. As shown in Fig. 12(a), as the piston descends to successfully engage the upper and lower-rotation sleeves, the formation applies a load to the piston through the rotational bit-drive mechanism, sacrificing the downward piston movement's energy. This instantaneously reduces the acceleration value from 222 to 189.2 m/s^2. This load persists during the downward impact on the drill bit. When the load reaches a certain threshold, it decelerates the piston's impact velocity or even halts its descent. Therefore, investigating the torque load's impact on the piston's impact energy is crucial.

5.4. Effect of torque load

Fig. 13 illustrates the relationship between the impact and torque performance of the Φ127NSH and torque load. It is shown that the impact performance, encompassing impact velocity U_p, frequency F, and maximum piston displacement L_p, exhibits a negative correlation with torque load T. Impact velocity, crucial for efficient impact drilling, is significantly influenced by torque load. Specifically, the impact velocity generated without torque load is 5.16 m/s, and when the torque load reaches 400 N·m, the impact velocity reduces to 3.98 m/s, which is 22.87% less than that without torque load. The impact frequency F and maximum piston displacement L_p experience marginal changes with torque load variation, diminishing by 3% and 1.5%, respectively, as torque T increases from 0 to 400 N·m.

Regarding torque performance, depicted in Fig. 13(d), under a 400 N·m torque load, the single rotational angle of the drill bit β and rotational speed n are 14.11° and 29.5 r/min, respectively, marking a 2.42% and 5.44% decrease from the without torque load state (14.46°, 31.2 r/min). Analysis based on Eqs. (1) and (2) reveals a positive correlation between the single rotation angle and maximum piston displacement, with rotation speed determined by their product. Since maximum piston displacement and frequency exhibit minimal sensitivity to torque load, its effect on the single rotational angle of the drill bit and rotational speed is minimal.

Furthermore, the pressure drop ΔP was increased by the applied torque load, albeit non-significant, from 0.87 to 0.88 MPa, indicating a 1.15% increase. In summary, torque load primarily impacts the impact velocity, with minimal influence on other parameters.

The cause can be attributed to the variations in piston velocity and acceleration, as displayed in Fig. 14. The resistance exerted on the piston descent was relatively high when the torque load T was larger, and other parameters were constant. This resulted in a notable reduction in the downward piston acceleration, from 225.75 to 149.76 m/s^2, as shown in Fig. 14(i). Consequently, the impact velocity U_p decreased with increasing T. Furthermore, within region (ii), elevating the T value reduces the initial velocity in the cycle from 1.27 to 0.98 m/s, resulting in a lower accumulation of initial kinetic energy by the piston throughout the cycle. This accounts for the fact that the maximum displacement of the piston L_p decreases with T increasing. Lower L_p results in a shorter acting distance of the high air pressure within the rear chamber, consequently decreasing the U_p. Furthermore, F reduces as the period increases with the increase in T value.

5.5. Effect of engagement distance of the rotation sleeves

The engagement distance of the rotation sleeves L_{ed} serves as a pivotal parameter in the unique built-in rotational mechanism of the NSH self-rotating pneumatic hammer. It signifies the point at which the upper and upper-rotation sleeves effectively engage after the piston has descended a specific distance, as depicted in Figs. 2 and 3, which marks the beginning of bearing torque and rotating the drill bit. Numerical simulations were conducted to evaluate the hammer's impact and torque performance under varying rotation sleeve engagement distances, as shown in Fig. 15. Remarkably, the applied torque of 300 N·m was chosen to elucidate the torque's impact on the Φ127NSH's performance. Impact performance (U_p, F, L_p) exhibited a positive correlation with L_{ed}. Increasing L_{ed} from 10 to 85 mm resulted in a 25.26% rise in impact velocity U_p, from 3.88 to 4.86 m/s. Correspondingly, maximum piston displacement L_p and impact frequency F increased slightly from 108.54 to 109.75 mm and from 12.39 to 12.87 Hz, respectively, by 1.1% and 3.9%. It is evident that impact velocity U_p, a key indicator for rock fracturing, is notably influenced by L_{ed}. Conversely, torque performance (β, n) displayed a negative correlation with L_{ed}, with a significant effect. For instance, at L_{ed} of 85 mm compared to 10 mm, single rotational angle of the drill bit β decreased from 20.3° to 5.1°, while rotational speed n decreased from 41.9 to 10.9 r/min, marking reductions of 74.9% and 73.9%, respectively.

This finding the trade-off between impact and torque performance with varying engagement distance of the rotation sleeves L_{ed}. Balancing these aspects is crucial for optimizing the distance L_{ed} to achieving better overall performance. Additionally, while the pressure drop ΔP exhibited a negative correlation with L_{ed}, the decrease from 0.88 to 0.87 MPa, with a slight decrease of 1.14%.

The cause can be attributed to the changing of the piston acceleration. A larger engagement distance L_{ed} delays the onset of the engagement distance begins to be exerted on the piston, resulting

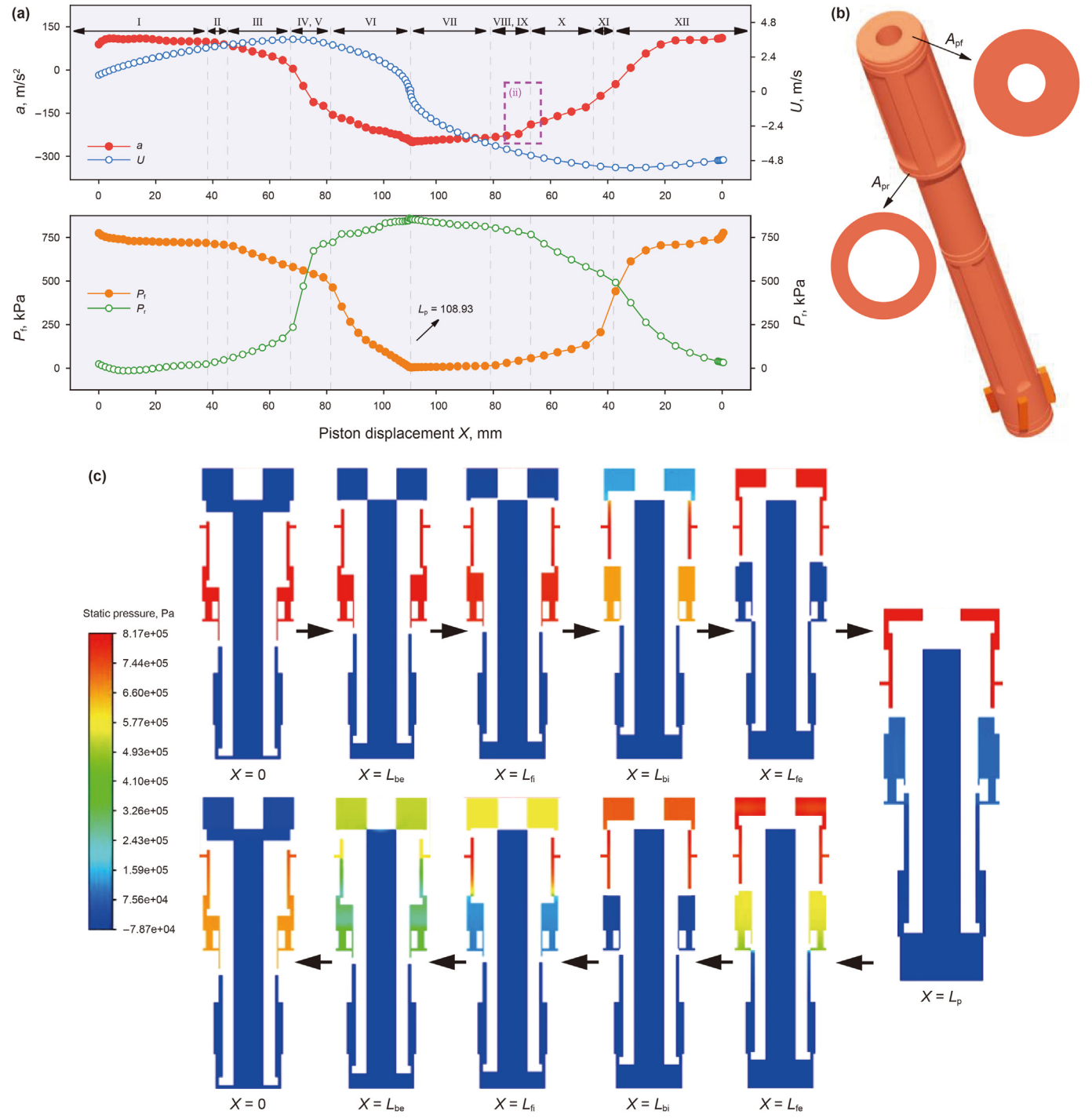

Fig. 12. (**a**) Velocity and acceleration of the piston, pressure in chamber vs. time profiles, (**b**) area of the piston exposed to the chambers, and (**c**) simulated pressure contours for each phase. (Group #2, $\theta = 0°$).

in a later sharp reduction in the acceleration of the descending piston, as displayed in Fig. 16. This implies a reduction in the resistance distance of the engagement distance acting on the piston during its downward motion, and more gas energy is utilized to drive the piston downward, thereby enhancing the piston's impact velocity. Meshing distance only affects the distance of torque action on the piston, and the remaining phases of the piston experience essentially the same force. Therefore, the variations in both the maximum piston displacement and the impact frequency are small.

Furthermore, according to Eq. (1), the common influence of the increasing engagement distance and the insignificant change of the maximum displacement leads to a significant decrease in the effective movement distance of the piston in the rotating sleeve, which further leads to a significant decrease of the single rotational angle of the drill bit. Considering that the impact frequency of the drilling tool does not change significantly with the engagement distance, the final rotational speed of the self-rotation hammer also decreases with the increase of the L_{ed}.

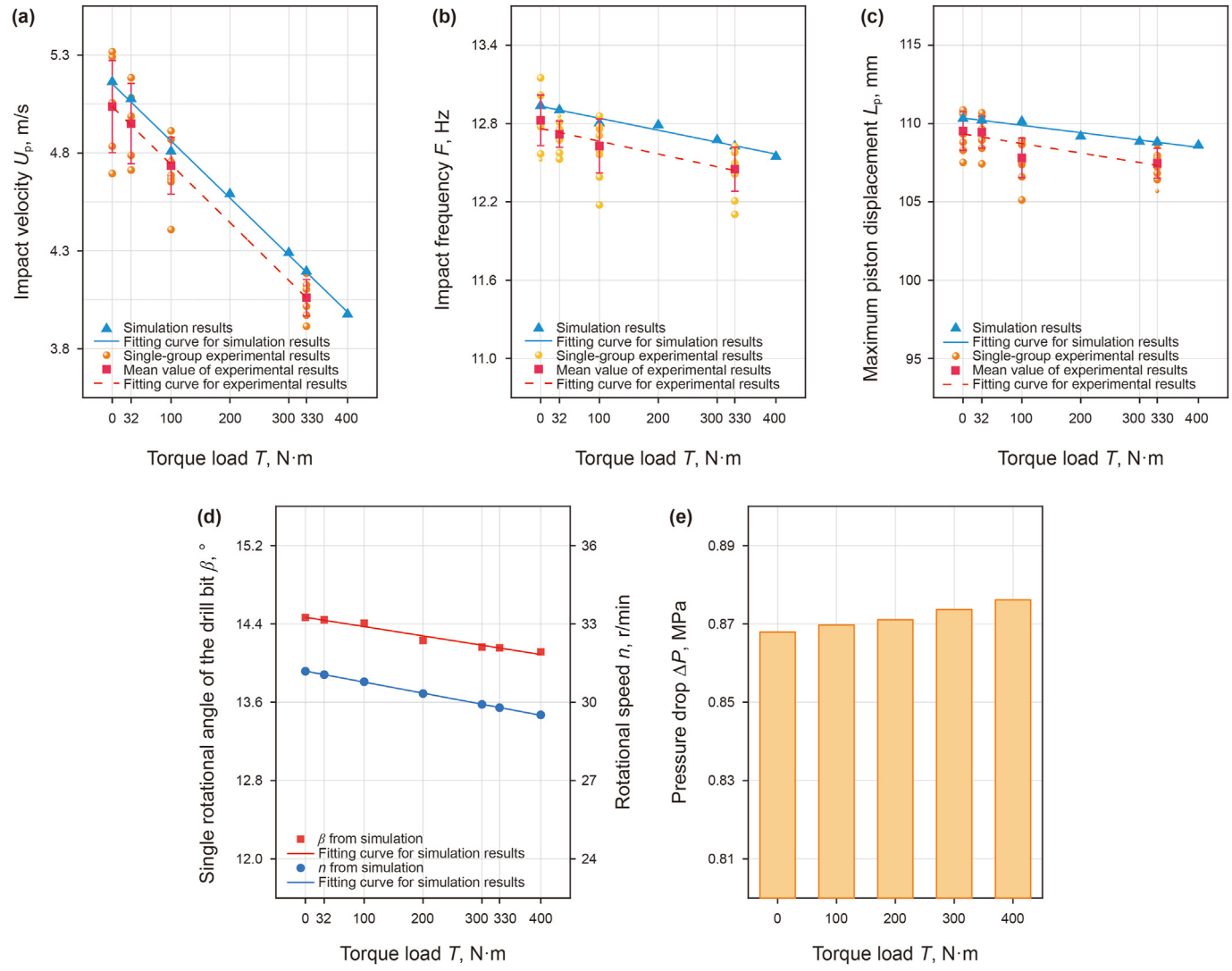

Fig. 13. Relationship between impact and rotational performance of the NSH and torque load: (**a**) impact velocity, (**b**) impact frequency, (**c**) maximum piston displacement, (**d**) single rotational angle of the drill bit and rotational speed, and (**e**) pressure drop (#3 in Table 3).

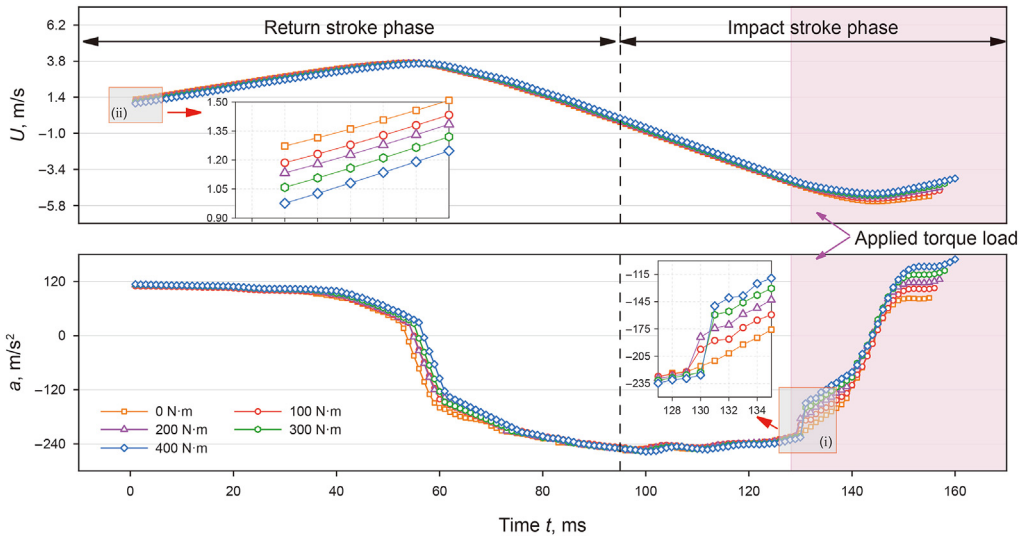

Fig. 14. Piston velocity and acceleration vs. time under differential torque load.

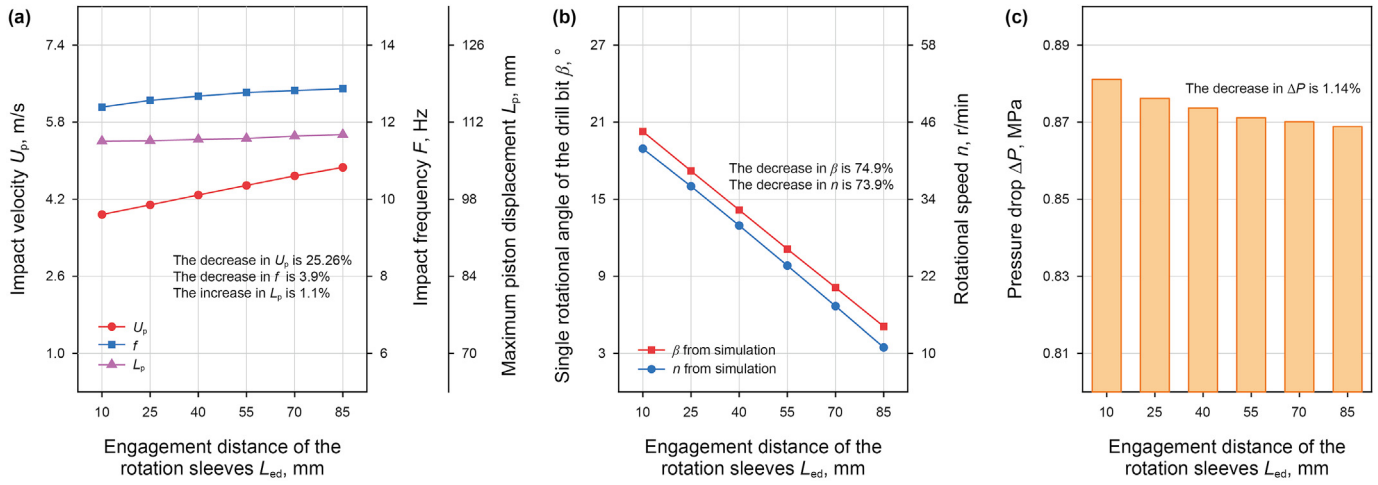

Fig. 15. Relationship between the piston performance and engagement distance in rotary sleeve from simulations. (**a**) impact velocity, frequency and maximum piston displacement, (**b**) single rotational angle of the drill bit and rotational speed, and (**c**) pressure drop (#4 in Table 3).

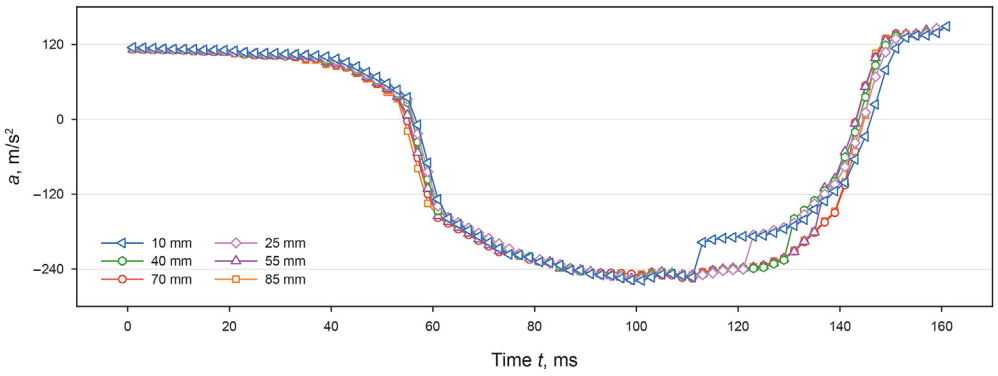

Fig. 16. Piston acceleration vs. time profiles under differential engagement distance in rotary sleeve from simulation.

5.6. *Effect of well deviation angle*

Self-rotation pneumatic hammers rely on pistons undergoing periodic reciprocation driven by gas to achieve 'impact' and 'rotary' functions, as discussed in Section 2.1. During drilling operations in directional wells with varying deviation angles, the gravitational energy storage and frictional resistance of the piston will change, subsequently influencing the piston's motion characteristics, according to Eq. (10). Thus, the hammer's output performance under varying well deviation angles was investigated, with the

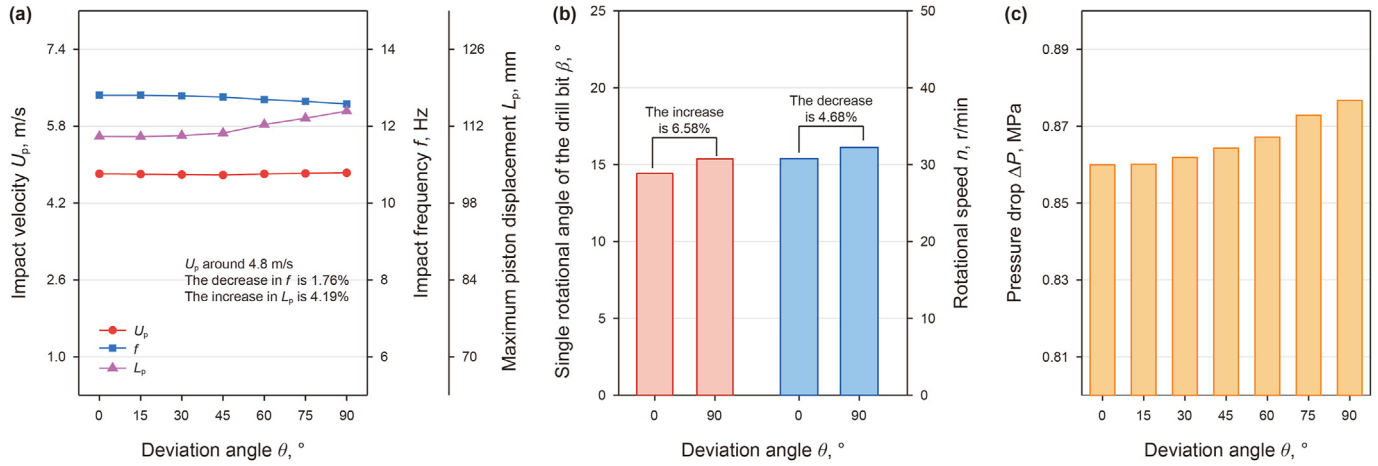

Fig. 17. Relationship between the impact and rotational performance of the piston and deviation angle. (**a**) impact velocity, impact frequency, and maximum piston displacement, (**b**) single rotational angle of the drill bit and rotational speed, and (**c**) pressure drop (#2 in Table 3).

corresponding relationship shown in Fig. 17. The impact velocity U_p appears to be minimally affected by the deviation angle θ, remaining consistent at around 4.8 m/s. The pressure drop ΔP, and maximum displacement L_p are positive with the deviation angle θ. When θ rises from 0° to 90°, L_p and ΔP increased from 110.13 to 114.74 mm and 859.94 to 876.69 kPa, respectively, representing a rise of 4.19% and 1.95%. Conversely, the impact frequency was negatively correlated with the well inclination angle, dropping from 12.8 to 12.58 Hz, a decrease of 1.76% and, consequently, based on Eqs. (1) and (2), the single rotational angle of the drill bit and rotational speed β and rotational speed n experience a slight increase of 6.58% and 4.68%, respectively. Thus, the performance variation of the self-rotating pneumatic hammer is minimal when drilling directional wells with varying deviation angles.

The performance variations can be explained by the changes in the frictional force exerted on the piston F_f, and the component on the axial axis of the piston's gravity G_a, as illustrated in Fig. 18. The G_a and F_f act as resistance to the downward movement of the piston according to Eq. (9), and their values both reduce as the deviation angle θ increases, reducing from 215.6 to 21.56 N. The reduced resistance during the piston's ascent pushes it to a farther position, as depicted in Fig. 17(a).

Increasing the maximum piston displacement L_p extends the distance over which high air pressure within the rear chamber acts as the piston descends, consequently resulting in a higher impact velocity U_p. However, according to Eq. (9), G_a acts as the driving force for the descending piston, while F_f serves as the resistance force. Their vector sum in the downward direction of the piston decreases as the deviation angle θ increases, reducing from 215.6 to −21.56 N, as displayed in Fig. 18. This causes the piston acceleration to decrease, which reduces the U_p. It is evident that a larger θ corresponds to a smaller driving force, resulting in a lower U_p. Thus, the combined effect of both causes U_p to exhibit a slight increase, approaching a stable trend, as shown in Fig. 17(a).

Furthermore, F is primarily influenced by U and L_p. As shown in Fig. 17(a), L_p increases with the increase of θ, and U_p remains stable. The increase in L_p results in an extended piston movement distance, thereby reducing the impact frequency F. Thus, with an increase in θ, F tends to decrease, as depicted in Fig. 17(b).

Notably, as the well deviation angle rises from 0° to 90°, the resultant force decreases by 194.04 N in the return stroke and 237.16 N in the impact stroke, as seen in Fig. 18. According to Eq. (10), this has a minimal impact on the acceleration, with changes of only 8.82 and 10.78 m/s^2, compared to the variation in acceleration under the influence of pressure, gravity, and frictional forces (−250.57, 111.39), as discussed in Section 5.2. This explains the relatively small change in the piston performance. Furthermore, it indicates that with a smaller mass-flow rate, the pressure dynamic force contributes less to the acceleration. Conversely, the frictional force exerted on the piston F_f, and the component on the axial axis of the piston's gravity G_a account for a greater proportion, resulting in a greater impact on the acceleration and, consequently on the piston's output performance. As shown in Fig. 8, there is a 16.5% reduction in U_p, a 12.6% decrease in F, and a 9.11% increase in L_p at a flow rate of 0.06 kg/s, compared to 0.18 kg/s.

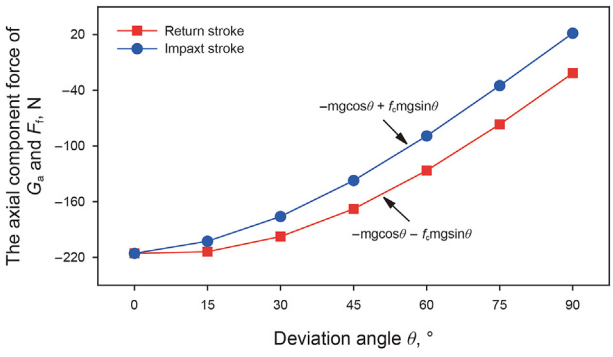

Fig. 18. The component axial forces of gravity and friction on the piston.

6. Conclusion

A novel structure for self-rotating pneumatic hammer was proposed in this study. Numerical modeling of airflow dynamics and resulting piston movement within the NSH was conducted using ANSYS Fluent. The ability of the Φ127NSH to drill into granite without rotating the drill pipe was analyzed. Subsequently, a mechanism of piston motion was provided, along with a numerical investigation into the influence of torque load, engagement distance of the rotation sleeves, and deviation angle on both the impact and rotational performance of the NSH in detail. The main contributions and conclusions of this study are listed below:

(1) The experimental results of Φ127NSH drilling granite indicate that the proposed Φ127NSH successfully realizes both the functions of impact and rotary drill bit, and granite smoothly feeds to form a clear crushed pit and a continuous shear rock zone. In addition, the borehole wall is smoothed by the shearing and grinding action of the edge teeth of the drill bit.
(2) The established numerical method can accurately capture the piston's real-time motion within the NSH, and obtain its output performance values, including impact performance (impact velocity, impact frequency, maximum piston displacement), rotational performance (single rotational angle of the drill bit, rotational speed), and pressure drop. The maximum error between simulated and experimental data is 8.2%.
(3) The torque load adversely affects the NSH output performance. Increasing engagement distance improves impact performance while reducing torque performance. The performance variation of the NSH is minimal when drilling directional wells with varying deviation angles. The designed Φ127NSH operates at an impact velocity of 3.98 m/s, impact frequency of 12.55 Hz, and rotational speed of 29.51 r/min under a mass-flow rate of 0.18 kg/s, torque load of 400 N·m, engagement distance of 40 mm, and well deviation angle of 0°.

In future research, the performance of the proposed self-rotating pneumatic hammer in field drilling tests will be further explored and compared with existing ones. Additionally, the strength of the internal mechanisms and the rock fragmentation mechanisms of the NSH during operation will be analyzed.

CRediT authorship contribution statement

Jin-E Cao: Writing – original draft, Visualization, Validation, Data curation. **Hong-Yu Cao:** Writing – original draft, Validation. **Hong-Yun Zhang:** Validation, Methodology. **Jin-He Bai:** Validation. **Pin-Lu Cao:** Writing – review & editing, Methodology, Funding acquisition.

Declaration of competing interest

The authors declare that they have no known competing financial interests or personal relationships that could have appeared to influence the work reported in this paper.

Acknowledgement

The authors thank the anonymous reviewers and editors for their inspiring remarks and comments. This study was supported by the Natural Science Foundation of Jilin Province (YDZJ202101ZYTS143).

References

ANSYS Inc, 2020. ANSYS Fluent Theory Guide, 2020R2.

Barbosa, L.F.F., Nascimento, A., Mathias, M.H., de Carvalho Jr, J.A., 2019. Machine learning methods applied to drilling rate of penetration prediction and optimization-A review. J. Pet. Sci. Eng. 183, 106332. https://doi.org/10.1016/j.petrol.2019.106332.

Bo, K., Chen, B.Y., Hu, Y., Wang, M.S., 2022. Design optimization and feasibility analysis of pneumatic DTH hammer with self-rotation bit. J. Vibroengineering. 24 (2), 305–316. https://doi.org/10.21595/jve.2022.22276.

Bournet, P.E., Rojano, F., 2022. Advances of Computational Fluid Dynamics (CFD) applications in agricultural building modelling: research, applications and challenges. Comput. Electron. Agric. 201, 107277. https://doi.org/10.1016/j.compag.2022.107277.

Bui, H.D., Meyers, J.A., Yost, A.B., 1997. Introduction of Steerable Percussion Air Drilling System. SPE Annu. Tech. Conf. Exhib. SPE-38582-MS. https://doi.org/10.2118/38582-MS.

Cao, J.E., Cao, P.L., Wen, C.D., Cao, H.Y., Yao, S.S., Yin, Q.L., 2024. Multi-objective niching quantum genetic algorithm-based optimization method for pneumatic hammer structure. Expert Syst. Appl. 238, 122047. https://doi.org/10.1016/j.eswa.2023.122047.

Cao, P.L., Cao, H.Y., Cao, J.E., Wen, C.D., Chen, B.Y., Yao, S.S., 2023. Performance of large-diameter pneumatic down-the-hole (DTH) hammers: a focus on influences of the hammer structure. Petrol. Sci. 20 (4), 2399–2412. https://doi.org/10.1016/j.petsci.2023.02.028.

Chervov, V.V., 2020. Expansion of application range of pneumatic hammers with adjustable impact effect. IOP Conf. Ser. Earth Environ. Sci. 523 (1), 012021. https://doi.org/10.1088/1755-1315/523/1/012021.

Chiang, L.E., Stamm, E.B., 1998. Design optimization of valveless DTH pneumatic hammers by a weighted pseudo-gradient search method. J. Mech. Des. 120 (4), 687–694. https://doi.org/10.1115/1.2829332.

Dixon, A.G., Partopour, B., 2020. Computational fluid dynamics for fixed bed reactor design. Annu. Rev. Cell Biol. 11 (1), 109–130. https://doi.org/10.1146/annurev-chembioeng-092319-075328.

Gao, Z.L., Wang, Y.L., Su, Y., Chen, L., 2019. Validation of a combined dynamic mesh strategy for the simulation of body's large amplitude motion in wave. Ocean Eng. 187, 106169. https://doi.org/10.1016/j.oceaneng.2019.106169.

He, C., Han, L.X., Chen, X.B., Chen, L., 2011. Development of air hammer with self-propelled round bit and the contact analysis of the key components. Adv. Mater. Res. 339, 243–249. https://doi.org/10.4028/www.scientific.net/AMR.339.243.

He, J.F., Sun, B.X., Liang, Y.P., Luo, Y.J., 2018. Research on suction capacity and dust suppression performance of a reverse circulation air hammer in tunnel drilling. Tunn. Undergr. Space Technol. 71, 391–402. https://doi.org/10.1016/j.tust.2017.09.008.

Hu, G., Huang, X.Q., Liu, X.Y., Meng, Q.K., 2015. Application limitations and future development directions of air hammer drilling technology. In: Proceedings of the 2015 International Symposium on Material, Energy and Environment Engineering, pp. 498–501. https://doi.org/10.2991/ism3e-15.2015.119.

Inglis, T., 2013. Directional Drilling, 2. Springer Science & Business Media.

Kim, D.J., Oh, J.Y., Cho, J.W., Kim, J., Chung, J., Song, C., 2019. Design study of impact performance of a DTH hammer using PQRSM and numerical simulation. J. Mech. Sci. Technol. 33, 5589–5602. https://doi.org/10.1007/s12206-019-1052-0.

Kondratenko, A.S., Timonin, V.V., Patutin, A.V., 2016. Prospects for directional drilling in hard rocks. J. Min. Sci. 52, 129–134. https://doi.org/10.1134/S1062739116010212.

Kong, Y., Guan, M.F., 2023. Hydro-mechanical simulations aid demand-oriented design of slit dams for controlling debris flows, debris avalanches and rock avalanches. Eng. Geol. 326, 107314. https://doi.org/10.1016/j.enggeo.2023.107314.

Li, W., Huang, G.L., Yu, F., Ni, H.J., Jiang, W., Zhang, X.B., 2020. Modeling and numerical study on drillstring lateral vibration for air drilling in highly-deviated wells. J. Pet. Sci. Eng. 195, 107913. https://doi.org/10.1016/j.petrol.2020.107913.

Li, Y.L., Peng, J.M., Zhang, P.Y., Huang, C.Y., 2021a. Hard rock fragmentation in percussion drilling considering confining pressure: insights from an experimental study. Int. J. Rock Mech. Min. Sci. 148, 104961. https://doi.org/10.1016/j.ijrmms.2021.104961.

Li, Z.S., Cao, K., Li, X.B., Chen, R., 2021b. Computational fluid dynamics modeling of spatial atomic layer deposition on microgroove substrates. Int. J. Heat Mass Tran. 181, 121854. https://doi.org/10.1016/j.ijheatmasstransfer.2021.121854.

Liu, Q.Y., Tang, Y., Wang, D.G., Xie, C., 2015. Numerical simulation on the impact dynamics of a novel rotation air hammer and experimental research. J. Vibroengineering. 17 (5), 2260–2271.

Ma, T.S., Chen, P., Zhao, J., 2016. Overview on vertical and directional drilling technologies for the exploration and exploitation of deep petroleum resources. Geomech Geophys Geo 2, 365–395. https://doi.org/10.1007/s40948-016-0038-y.

Pletcher, J., Scarr, A., Smith, J., Swadi, S., Rogers, C., 2010. Application of air percussion drilling improves drilling efficiency in horizontal sandstone wells. In: SPE Annual Technical Conference and Exhibition. SPE-135308-MS. https://doi.org/10.2118/135308-MS.

Wang, Y., Zhong, K., Zhang, N.B., Kang, Y.M., 2014. Numerical analysis of solar radiation effects on flow patterns in street canyons. Eng. Appl. Comput. Fluid Mech. 8 (2), 252–262. https://doi.org/10.1080/19942060.2014.11015511.

Xi, Y., Wang, W., Fan, L.F., Zha, C.Q., Li, J., Liu, G.H., 2022. Experimental and numerical investigations on rock-breaking mechanism of rotary percussion drilling with a single PDC cutter. J. Pet. Sci. Eng. 208, 109227. https://doi.org/10.1016/j.petrol.2021.109227.

Xiong, Q.S., Ye, Y.S., Liu, S.L., Li, J., Kong, F.J., 2011. The computerized simulation software development of the bidirectional pneumatic hammer. Appl. Mech. Mater. 90, 1345–1350. https://doi.org/10.4028/www.scientific.net/AMM.90-93.1345.

Yakhot, V., Orszag, S.A., Thangam, S., Gatski, T.B., Speziale, C.G., 1992. Development of turbulence models for shear flows by a double expansion technique. Phys. Fluids 4 (7), 1510–1520. https://doi.org/10.1063/1.858424.

Yin, Y., 2020. Pneumatic down-the-hole hammer. High Speed Pneumatic Theory and Technology Volume II: Control System and Energy System: 195–268. Springer, Singapore.

Zhang, X.X., Luo, Y.J., Fan, L.M., Peng, J.M., Yin, K., 2019. Investigation of RC-DTH air hammer performance using CFD approach with dynamic mesh method. J. Adv. Res. 18, 127–135. https://doi.org/10.1016/j.jare.2019.02.001.

Zhang, Z., Zhang, W., Zhai, Z.J., Chen, Q.Y., 2007. Evaluation of various turbulence models in predicting airflow and turbulence in enclosed environments by CFD: Part 2-Comparison with experimental data from literature. HVAC R Res. 13 (6), 871–886. https://doi.org/10.1080/10789669.2007.10391460.

Zhao, D.J., Sun, Z.H., Liu, H.N., Gan, X., Yu, H., 2016. Experimental application on reverse circulation drilling technology with DTH air hammer in an open pit mine in Sichuan. Int. J. Earth Sci. 9 (3), 906–911.

Zhao, Z., Meng, Y.F., Li, Y.J., Shi, X.C., Xiang, C.L., 2015. Effects of working angle on pneumatic down-the-hole hammer drilling. Rock Mech. Rock Eng. 48, 2141–2155. https://doi.org/10.1007/s00603-014-0667-9.